Acta Cryst. (1978). A**34**, 103–112

Computed Electron Microscope Images of Atomic Defects in F.c.c. Metals

BY P. M. FIELDS AND J. M. COWLEY

Department of Physics, Arizona State University, Tempe, Arizona 85281, *USA*

(*Received* 15 *April* 1977; *accepted* 6 *August* 1977)

The bright-field and dark-field electron microscope images expected for [100] split interstitials in thin crystals of gold and aluminum without and with lattice relaxation have been calculated by the method of periodic continuation including full *n*-beam dynamical interactions of both the Bragg reflections and the diffuse scattering. The advantage of using 1 MeV rather than 100 keV electrons is demonstrated in that, even with the same nominal resolution, the 1 MeV electrons give images in which the defect structure is more readily recognized. The conditions have been determined for which the defect images have high contrast and provide clear representations of the atom configurations.

1. Introduction

Results from high-resolution transmission electron microscopy have demonstrated that the electron scattering power of single heavy atoms is sufficient to allow their direct visual observation (Crewe, Wall & Langmore, 1970; Iijima, 1976, 1977). Since atomic defects in metals, such as vacancies and interstitials, should have comparable scattering power, these should also be detectable with present-day instruments. However there is no clear evidence that experimental observations of such defects have been made. We have therefore undertaken the simulation of defect images and diffraction patterns by computer calculation in order to determine the experimental conditions necessary for the recognition of atomic defects by direct imaging.

Apart from the instrumental factors which limit resolution, there are sources of confusion such as specimen surface structure and contamination which will make the recognition of defect images difficult. While it should be possible to obtain maxima or minima in image intensity with contrast values of 10 to 30% with current microscopes, it may be necessary to improve both the resolution and contrast in order to distinguish features of the images characteristic of the form of the defect or of the displacements of the surrounding atoms. Because the use of higher voltages offers the necessary improvements in resolution and contrast (Cowley, 1975*a*) we have made calculations for both 100 keV and 1 MeV electrons.

As a representative type of atomic defect, we consider the [100]-type split interstitial in face-centered cubic metals. These have been shown theoretically and by X-ray diffraction methods (Haubold, 1975) to be present in aluminum. The calculations for aluminum and gold may serve to test speculations on the imaging of local defects in general even though they may not represent conditions which are immediately accessible experimentally.

The calculation of high-resolution images of crystal defects, especially with such strongly scattering atoms as gold, presents difficulties which have led to the use of unsatisfactory approximations in the past. The use of the column approximation and a few-beam, perfect-crystal calculation (Bourret, Desseaux & Renault, 1975) is clearly inadequate since it cannot deal with the addition, subtraction or large local displacement of atoms. The assumption of kinematical scattering by the defect (Krakow, Chang & Sass, 1977) is inappropriate. It has been shown (*e.g.* Fisher, 1965; Cowley & Murray, 1968) that diffuse scattering intensities can be modified by at least an order of magnitude by the dynamical scattering in thin crystals of gold.

It is necessary to use a full dynamical theory which correctly includes the dynamical interactions of both the strong Bragg reflections due to the host lattice and the diffuse scattering arising from the deviations from periodicity.

2. Computing methods

The basis of the present calculations is the Cowley & Moodie (1957) multislice *n*-beam dynamical diffraction theory, adapted for numerical analysis by computer as discussed by Goodman & Moodie (1974). The computer program used was written by Skarnulis (1975) and has been modified and expanded by M. A. O'Keefe. Results using this program for calculating perfect crystal images have been presented by Skarnulis, Iijima & Cowley (1976) and O'Keefe & Anstis (in preparation). Features of primary interest in this program are the capability to include dynamical scattering among 3000 Bragg beams, to compute and store projected potentials of different structures in order to model specimen structure as a function of crystal thickness, and to produce half-tone displays of both diffraction pattern and image. To calculate the results presented in this paper 961 structure amplitudes were computed for

both the perfect and defect crystal structures. Initially 496 phase-grating amplitudes, corresponding to the projected potentials for slices of a perfect crystal and a crystal containing a [100]-type interstitial, were generated by convolution among the structure amplitudes. Diffraction by a crystal containing a defect is modelled by successive propagation of the electron wave and convolution of its amplitudes with the amplitudes of the appropriate phase gratings through the crystal in the incident beam direction.

The Fourier coefficients of the electron wavefunction at the exit face of the crystal may be squared and printed in half-tone to simulate the electron diffraction pattern. Images for various amounts of defocus were calculated using only those diffraction amplitudes lying within the objective-aperture radius, modified by the appropriate objective-lens aberrations. To display in greater detail the effect of dynamical scattering from [100]-type split interstitials on the diffraction intensities, calculations were also made using 889-beam phase-grating amplitudes.

Calculations in which relaxation of atoms in the neighborhood of the split interstitial is included were also performed using the same beam-number parameters. Numerical results are printed in addition to the half-tone displays when the program is executed so that quantitative evaluation of intensities is available.

In order to use this perfect-crystal multislice computer program to include the effects of the diffuse scattering by a nonperiodic defect structure the assumption of periodic continuation is employed. This involves localizing the model defect structure within an extended unit cell, convoluting this structure in the directions perpendicular to the incident beam by lattice vectors which are multiples of the (conventional cubic) unit-cell lattice vectors, and thereby generating a superlattice slice of defect structures. The utility of this concept in the practical matter of simulating electron diffraction patterns and electron microscope images from nonperiodic structures is discussed by Cowley (1975*b*; § 11.5), and has been applied by Grinton & Cowley (1971); Fejes (1973); Kuwabara & Uefuji (1975); Cockayne (1976) and Spence (1975, 1977).

In the context of the multislice approach to diffraction, the theoretical basis of periodic continuation is discussed below for the dynamical interaction between any two slices of a crystal, each of which may be unique and may contain a defect.

The amplitude for electron scattering at the $(n-1)$th slice in reciprocal space, $U_{n-1}(\mathbf{u})$, is given by the Fourier transform of the real space amplitude, $\psi_{n-1}(\mathbf{r})$, which is periodic in an extended lattice vector $\mathbf{S}_l$, *i.e.*

$$\mathscr{F}[\psi_{n-1}(\mathbf{r}) * \sum_l \delta(\mathbf{r}-\mathbf{S}_l)] = \sum_m U_{n-1}(\mathbf{u})\,\delta(\mathbf{u}-\mathbf{H}_m),$$

where $\mathbf{H}_m$ is the lattice vector reciprocal to $\mathbf{S}_l$.

To incorporate dynamical scattering $U_{n-1}(\mathbf{u})$ is multiplied by the free-field propagator for the nth slice, and convoluted by the reciprocal-space phase grating for the nth slice, $Q_n(\mathbf{u})$, which is related through a Fourier transform to the real-space phase grating $q_n(\mathbf{r})$, also periodic in $\mathbf{S}_l$. Thus,

$$\mathscr{F}[q_n(\mathbf{r}) * \sum_l \delta(\mathbf{r}-\mathbf{S}_l)] = \sum_m Q_n(\mathbf{u})\,\delta(\mathbf{u}-\mathbf{H}_m).$$

Analytically, the phase grating for the nth slice is given in the phase object approximation by

$$q_n(\mathbf{r}) = \exp[-i\sigma\varphi_n(\mathbf{r})\,\Delta z],$$

where

$$\sigma = (\hbar c\beta)^{-1}; \quad \Delta z = \text{slice thickness},$$

and

$$\varphi_n(\mathbf{r}) = \mathscr{F}^{-1}V_n(\mathbf{u})$$

is the projected potential for the nth slice.

$V_n(\mathbf{u})$ is a section in reciprocal space of the structure amplitudes for the nth slice of the extended unit cell, and is computed using the atomic scattering factors and positions of the atoms within the slice chosen to represent a section of the defect structure which is repeated with the periodicity of the superlattice unit cell.

It is to be emphasized that both $U_{n-1}(\mathbf{u})$ and $Q_n(\mathbf{u})$ given in the previous equations are continuous functions in reciprocal space since the introduction of a defect structure into a unit cell means that the transition probability for scattering from discrete reflections into the diffuse background is finite. The creation of a superlattice through periodic continuation generates a set of superlattice reflections which can be used to represent the continuum in the sense that the multiplication of $U_{n-1}(\mathbf{u})$ and $Q_n(\mathbf{u})$ by $\sum_m \delta(\mathbf{u}-\mathbf{H}_m)$ samples these functions in the intervals defined by $\mathbf{H}_m$. As the lateral dimensions of the extended unit cell containing the defect structure increase, the ideal case of a single defect situated in an otherwise perfect crystal slice is more closely approximated, and the reciprocal space is sampled at finer intervals for a more accurate representation of the diffuse elastic scattering. Of course, the perfect-crystal set of discrete beams is scaled by the same factors which multiply the real-space unit cell, and this implies a large increase in the number of beams required in the 'perfect-crystal' multislice routine.

This latter point can be most easily illustrated in the simple case where the conventional cubic unit cell forms the basis for defining the extended unit cell. The relevant parameters which are all interrelated are the number of diffraction beams used in the multislice calculation (N), the sampling interval (A^*), the lateral dimensions of the defect structure (D), the extended unit-cell dimensions (A), and the minimum resolvable distance ($\Delta X_{\min}$). Since D^{-1} is the dimension in reciprocal space to which the defect structure contributes scattered intensity, and if $1/n$ is the fractional part of D^{-1} considered to be important for sampling the

fluctuations of the continuous scattering, then

$$A^* = \frac{1}{nD} = \frac{1}{A} = \frac{1}{ma},$$

where m is the multiple of the real-space unit-cell dimension (a) used to define the extended unit cell. It also follows that

$$N = \left[\frac{2}{A^* \Delta X_{\min}} + 1 \right]^2.$$

As an example, for gold with a [100] split interstitial with a spacing between displaced atoms of 2 Å, an extended unit cell with dimensions $(2a,2a,a)$ was chosen, 496 beams were specified in performing the multislice dynamical scattering calculation, and consequently a sampling interval of 0·125 Å^{-1} and a minimum resolvable distance of 0·75 Å resulted. Since the actual image resolution depends on the number of diffracted beams included within the objective aperture for the imaging calculation, this latter figure is primarily useful as a guide in determining whether sufficient fundamental reflections are included in the multislice calculation to allow the dynamical scattering among diffuse and Bragg beams to be accurately represented.

It should be noted that the criteria used here for determining the adequacy of the calculations are quite different from those for images of defects obtained with relatively poor resolution ($\geq$10 Å) for which the usual calculations involve a column approximation. For the small atom displacements in strain fields extending over many unit cells around a defect the diffuse elastic scattering is sharply peaked around the Bragg reflection positions. It would be possible to use our multislice technique to calculate images for these cases but the sampling intervals would have to be very small, $\ll$0·1 Å^{-1}, a very large number of beams would be needed and the computing time would be excessive. The column approximation is useful in these cases. However for the large atom displacements around the defect center the column approximation is invalid. The diffuse scattering varies slowly through the entire region between reciprocal lattice points. Our multislice program is then appropriate and the sampling interval of 0·125 Å^{-1} is adequate to describe the relevant variations of diffuse scattering with sufficient accuracy.

The resolution figures quoted in the results are considered to be given by the reciprocal radius of the objective aperture used in the imaging calculation. The spherical aberration of the objective lens is usually considered as the factor limiting the resolution, but in practice it is usually necessary to include effects of chromatic aberration and beam divergence, whose cumulative effect can be represented by the replacement of the real aperture by a virtual aperture of reduced radius as shown by Anstis & O'Keefe (1976). Both the chromatic aberration and beam divergence were set to zero for the calculations presented, so the effects of inclusion of instrumental resolution-limiting parameters can be estimated by comparison with the predictions of the weak-phase-object approximation (kinematical scattering) as it is applied to the bright-field imaging problem (Cowley, 1975*b*; § 13.3). The resolution in this case is given by

$$\Delta X = 0{\cdot}66(C_s\lambda^3)^{1/4}$$

when the aperture radius and defocus are maximized and are given, respectively, by

$$u_{\max} = 1{\cdot}51(C_s\lambda^3)^{-1/4}; \quad \varepsilon_{\text{opt}} = -1{\cdot}15(C_s\lambda)^{1/2}.$$

The coefficient of spherical aberration was 1·8 mm throughout all calculations, so the former parameters at 100 keV are

$$\Delta X = 3{\cdot}64 \text{ Å}; \quad u_{\max} = 0{\cdot}275 \text{ Å}^{-1}; \quad \varepsilon_{\text{opt}} = -942 \text{ Å},$$

while at 1 MeV the corresponding results are

$$\Delta X = 1{\cdot}23 \text{ Å}; \quad u_{\max} = 0{\cdot}813 \text{ Å}^{-1}; \quad \varepsilon_{\text{opt}} = -457 \text{ Å}.$$

These numbers are suggestive, but agreement with the results (in particular the optimum-defocus values), certainly does not imply that the scattering can be treated kinematically.

The amounts of defocus employed also influence the size of the superlattice unit cell which should be used. The requirement is that within the defocus distance ε the spread of the electron wave due to Fresnel diffraction, given approximately by $(\varepsilon\lambda)^{1/2}$, should be much less than the superlattice unit-cell dimensions A. Alternatively, for a fixed value of A, the defocus $|\varepsilon|$ must be less than A^2/λ. In our case, $|\varepsilon| < A^2/\lambda = 1730$ Å for 100 keV or 7360 Å for 1 MeV electrons.

3. Results for Al and Au

A [100] split interstitial was situated in a unit cell with dimensions in the directions perpendicular to the incident beam that were twice those of the conventional cubic unit cell. The coordinates of the atoms of the interstitial were assumed to be $(\frac{3}{8},\frac{1}{2})$, $(\frac{5}{8},\frac{1}{2})$, relative to this large unit cell. Structure amplitudes and projected potentials (at 100 keV and 1 MeV) were computed for Al and Au for both the defect structure and the perfect crystal structure. The multislice routine was then used to compute through-focus series of bright-field electron microscope images and electron diffraction patterns for five slices of crystal, each slice being one unit cell thick and with the third slice containing the defect structure. Different objective aperture radii were used in the imaging computations in order to determine the combination of experimental parameters which resulted in the most easily interpretable image with the highest contrast. Contrast was determined by employing a program option which allows a 'densitometer' intensity trace to be taken across any portion

of the simulated electron micrograph. Additionally, dark-field images were computed using the artifice of setting fundamental diffraction intensities to zero prior to running the imaging routine.

Structure amplitudes and projected potentials were also computed for a defect structure which incorporated relaxation of atoms in the neighborhood of the split interstitial. No specific model was fitted to the displacement field, but rather the constraint imposed by periodic continuation was satisfied and resulted in an anisotropic distribution of relaxed atoms in the extended unit cell. In addition, this relaxation was restricted to the same slice as the split interstitial so that the displacements given to neighboring atoms are considered to be projected relaxation displacements. The displacements assumed ranged from 0·25 Å for nearest-neighbor atoms to zero at the superlattice cell boundaries.

Our model for the relaxation is admittedly very crude but this will not invalidate our general conclusions regarding image contrast, wavelength dependence and optimum defocus since these are quite insensitive to the details of the displacements assumed. The neglect of the z dependence of the relaxation is an approximation which is valid for these dynamical calculations providing that the large lateral atom displacements are confined to a region of thickness, depending on the resolution, for which the phase-object approximation is valid (about 10–15 Å in our case).

Figs. 1 to 19 show the results of our computations. Each picture displays two extended unit cells in the directions perpendicular to the [001] zone-axis orientation of the incident beam so the periodic continuation of the defect structure is apparent.

Figs. 1, 2 and 3 show the projected potentials at 1MeV of the perfect crystal, interstitial, and interstitial with relaxation structures, respectively. These results are part of the output in a multislice calculation, and provide a convenient means of visually determining the precise atom positions used in the structural model of defect structures. The calculated images represent the dynamical scattering between combinations of these projected potentials.

Figs. 4 and 5 show the 889-beam electron diffraction patterns (to 16th order in the [100] and [010] directions) of the split interstitial and the split interstitial

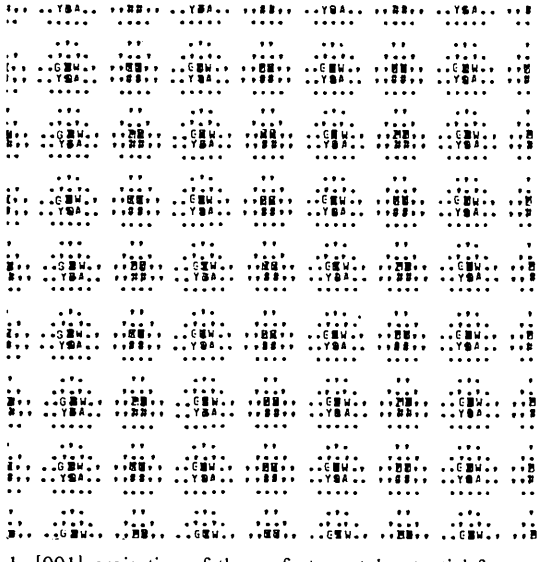

Fig. 1. [001] projection of the perfect-crystal potential for a gold crystal. Slight differences in detail between columns of peaks are related to the sampling interval of the printer.

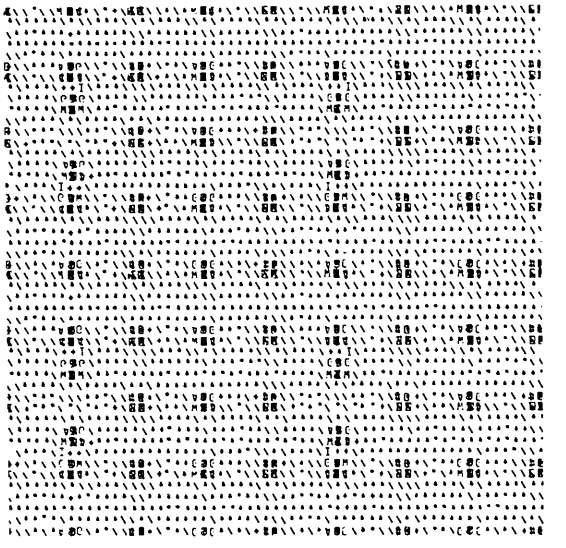

Fig. 2. Projected potential for a split interstitial located at $(\frac{3}{8},\frac{1}{2})$ $(\frac{5}{8},\frac{1}{2})$ in a 4 Å slice of gold crystal. Reference origin is at the upper left and the [100], [010] directions are down and right, respectively.

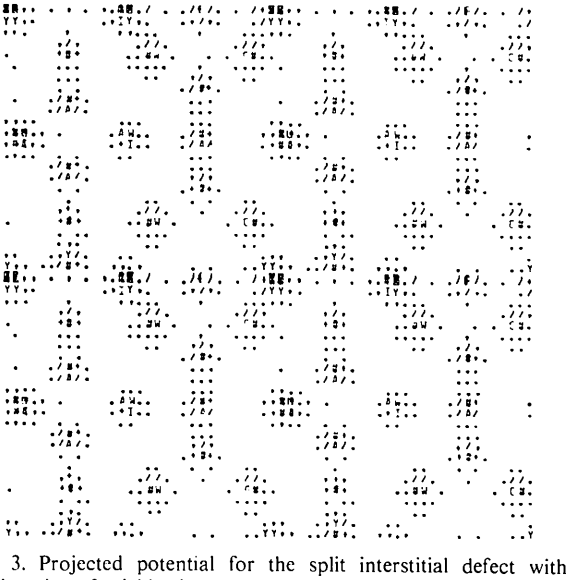

Fig. 3. Projected potential for the split interstitial defect with relaxation of neighboring atoms.

with relaxation. The intensities are displayed in reversed-contrast half-tone using a logarithmic scale in order to encompass the six-orders-of-magnitude ratio between the Bragg reflections and the diffuse background. This scaling emphasizes the distribution of diffuse elastic intensities in reciprocal space from each of the two defect structures. In particular, the dynamical effects on the diffuse scattering are clearly seen in Fig. 4. The kinematical approximation would give fringes $(2 \cos \pi a u - 1)^2$, attenuated by the square of the atomic scattering factor. Because of the dynamical scattering, the odd-numbered fringes are much weaker than the even-numbered ones.

Fig. 6 is the simulated image of the perfect crystal of Au at 1 MeV when the objective aperture was set at 1·097 $Å^{-1}$ and included 12 Bragg beams in the imaging process. The optimum value of defocus was determined to be −430 Å with a resulting contrast of 86%.

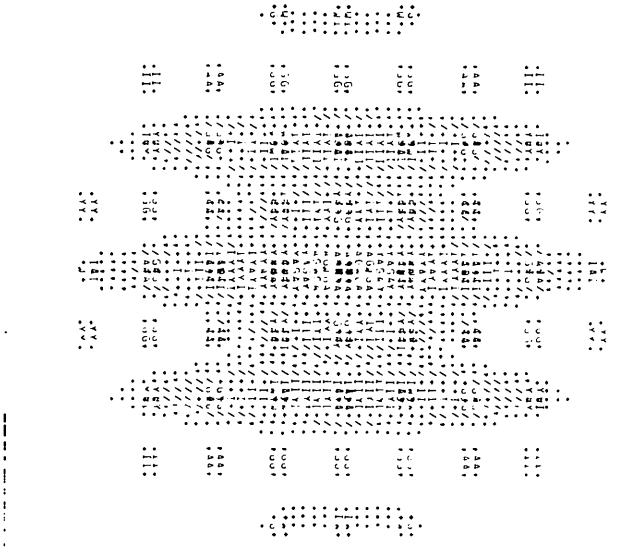

Fig. 4. Computed electron diffraction pattern for the split interstitial in a gold crystal, 20 Å thick; 100 keV (logarithmic intensity scale). Additional reciprocal lattice points have been included by interpolation between sampling intervals. References to coordinates in the text refer to reciprocal superlattice cells.

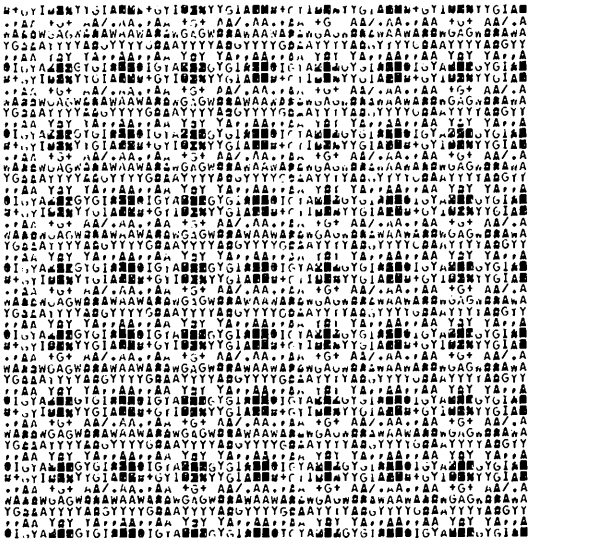

Fig. 6. Simulated 1 MeV electron microscope image of 20 Å Au perfect crystal (aperture radius u = 1·097 $Å^{-1}$; defocus ε = −470 Å).

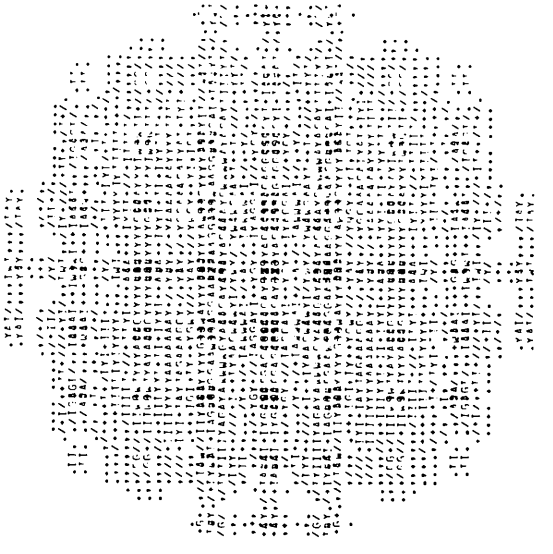

Fig. 5. Computed electron diffraction pattern for the split interstitial in gold, with relaxation.

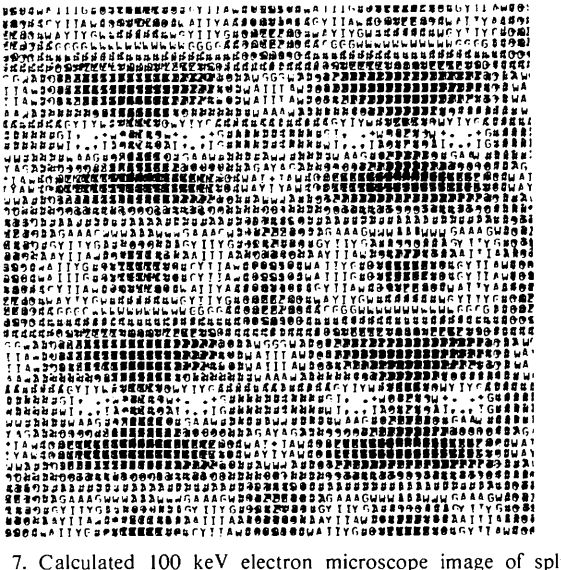

Fig. 7. Calculated 100 keV electron microscope image of split interstitial in Al crystal (u = 0·54 $Å^{-1}$; ε = −950 Å). The defect structure is repeated under the assumption of periodic continuation used in the calculations.

It is to be noted that the atom positions are characterized by a bright ring around a central dark spot similar to that observed in recent experimental results for the imaging of thin gold crystals at 100 keV (Hashimoto, Endoh, Tanji, Ono & Watanabe, 1976). This calculated, perfect-crystal image is a convenient standard in terms of contrast and atomic visibility against which to compare the images of the atomic defect structures. Figs. 7 and 8 are the 100 keV bright-field images of a split interstitial in Al and Au, respectively, when the objective aperture includes the largest possible amount of diffuse scattering while excluding the first-order fundamentals. The (nominal optimum) defocus for these images is −950 Å, and the recognizability of the atomic defect as a split interstitial is questionable. The corresponding 1 MeV images at a defocus of −470 Å are shown in Figs. 9 and 10, and it is apparent that an *a priori* statement about the atomic configuration of the defect structure is possible even at this reduced resolution (2·2 Å). Complementary to Figs. 8 and 10 are Figs. 11 and 12 which resulted when the central beam was set to zero prior to the imaging calculation, and which therefore represent the 100 keV and 1 MeV dark-field images of Au at defocus values of −350 and −270 Å, respectively. Fig. 11 is essentially uninterpretable in terms of the structure

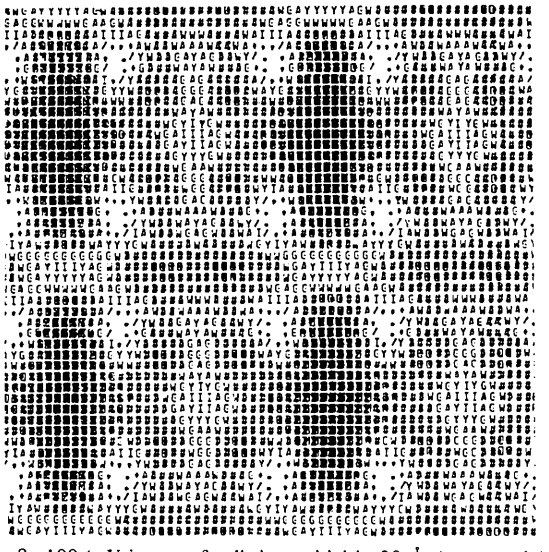

Fig. 8. 100 keV image of split interstitial in 20 Å Au crystal (u = 0·4425 Å^{-1}; ε = −950 Å).

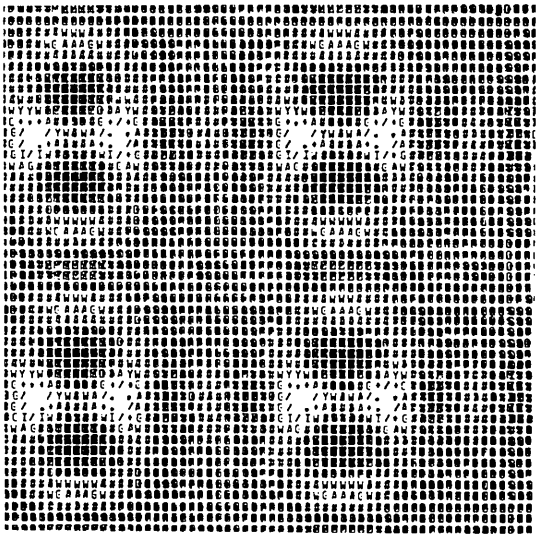

Fig. 10. 1 MeV image of Au split interstitial (u = 0·4425 Å^{-1}; ε = −470 Å).

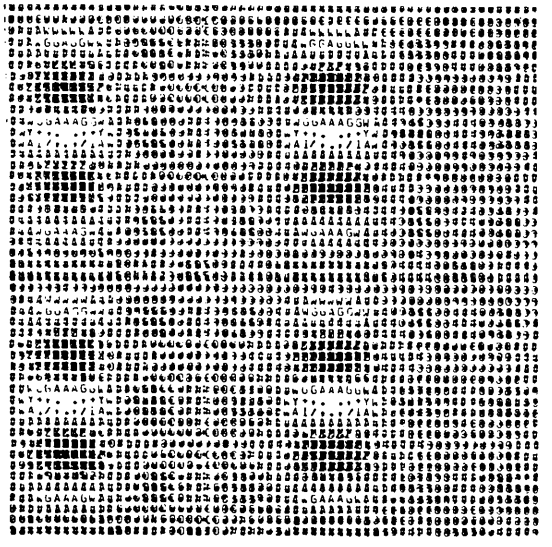

Fig. 9. Calculated 1 MeV electron microscope image of split interstitial in Al crystal (u = 0·45 Å^{-1}; ε = −470 Å).

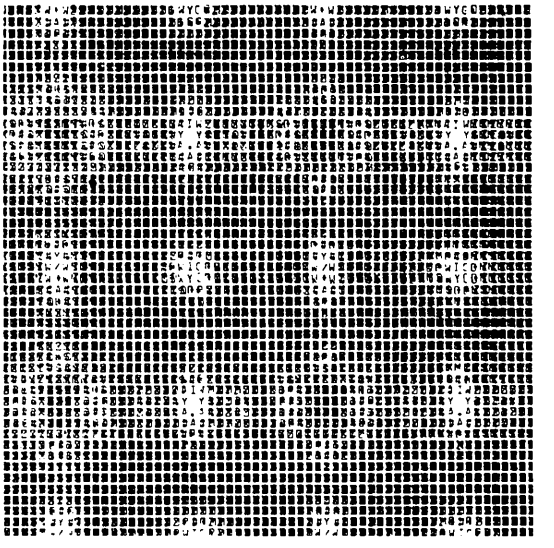

Fig. 11. 100 keV dark-field image of Au split interstitial (u = 0·4425 Å^{-1}; ε = −350 Å).

from which it was derived, and in particular the identification of white spots as corresponding to atoms is not possible. In contrast, the 1 MeV image of Fig. 12 demonstrates the value of higher voltage in dark-field imaging, as a unique characterization of structure can apparently be obtained. Since the use of a 1 MeV transmission electron microscope would also imply that larger objective apertures could be used to obtain improved resolution and contrast, the 1 MeV bright field images of the Al and Au split interstitial were also calculated for an aperture which included 12 Bragg beams (8th-order reflections in [100] and [010] directions), and are shown in Figs. 13 and 14. The optimum defocus for these images is −530 and −465 Å, respectively, and these values are significant because a through-focus perfect-crystal image series demonstrates that the defocus which optimizes defect contrast is also the defocus that minimizes the contrast of the host perfect-crystal structure. At higher resolution the calculated image must be coupled with the intensity trace option in order to evaluate quantitatively the contrast of the defect structure relative to the host structure features.

Effects of relaxation on image quality and interpre-

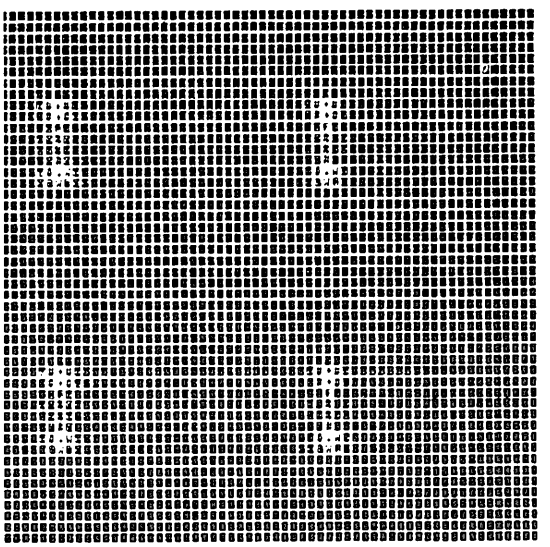

Fig. 12. 1 MeV dark field image of Au split interstitial (u = 0·4425 Å^{-1}; ε = −270 Å).

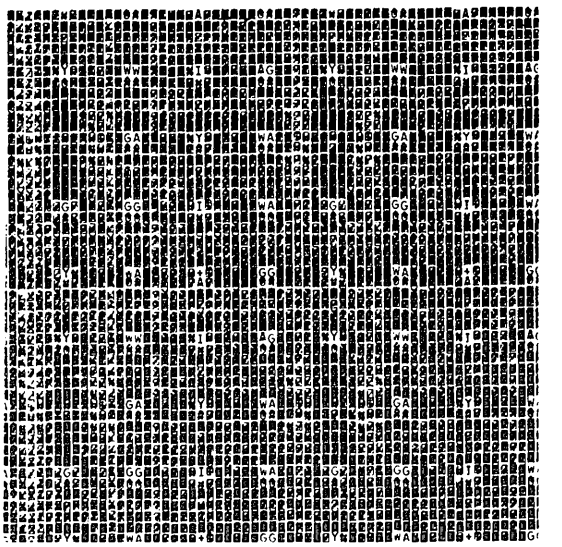

Fig. 14. 1 MeV image of Au split interstitial (u = 1·097 Å^{-1}; ε = −465 Å).

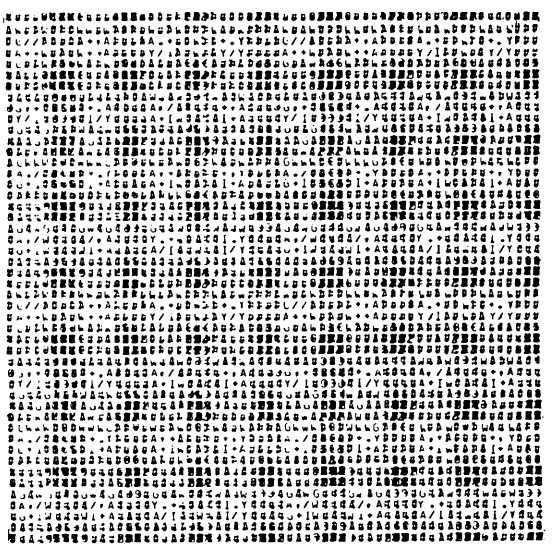

Fig. 13. Calculated 1 MeV electron microscope image of Al split interstitial (u = 1·1 Å^{-1}; ε = −530 Å).

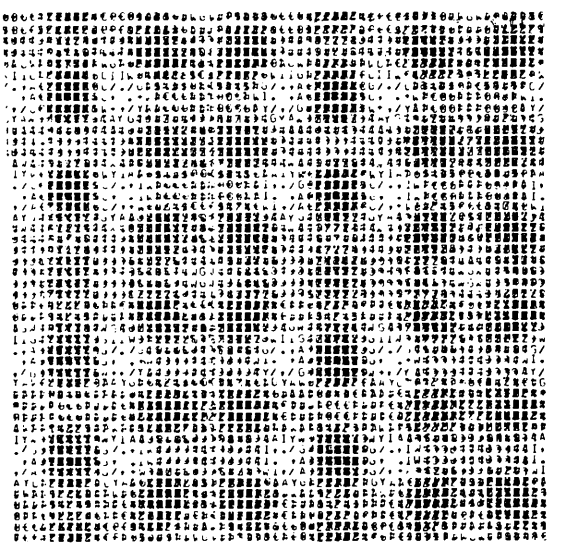

Fig. 15. Calculated 1 MeV electron microscope image of Al split interstitial with relaxation of the neighboring atoms (u = 0·45 Å^{-1}; ε = −470 Å).

tation are presented in Figs. 15 through 18. Figs. 15 and 16 should be referred back to 2 and 3, and compared to Figs. 9 and 10. In Figs. 15 and 16 both the split interstitial and the deviations from periodicity due to relaxation are readily identified. Information on perturbations of local crystal structure by an atomic defect may therefore be determined, although it must be realized that the displacement of atoms from their lattice positions now show up as minima at the lattice sites plus maxima at the new atom positions since the diffuse scattering comes from deviations from the average, periodic structure. Similarly, Figs. 17 and 18 can be related to 13 and 14, but the degradation of the image which includes relaxation at higher resolution does not permit meaningful interpretation of the defect structure. More extensive calculations using much larger extended unit cells with more elaborate relaxation schemes should be done to confirm these results.

Contrast values which can be expected at 100 keV and 1 MeV for Al and Au defects at 2·2 Å and 0·91 Å resolutions are indicated in Table 1. An example of the output generated by the 'densitometer' program option from which the tabulated data were determined is shown in Fig. 19.

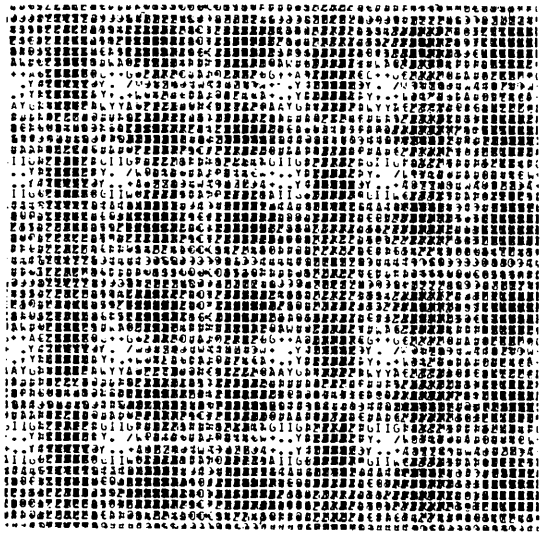

Fig. 16. 1 MeV image of Au split interstitial with relaxation of neighboring atoms ($u = 0{\cdot}4425$ Å^{-1}; $\varepsilon = -500$ Å).

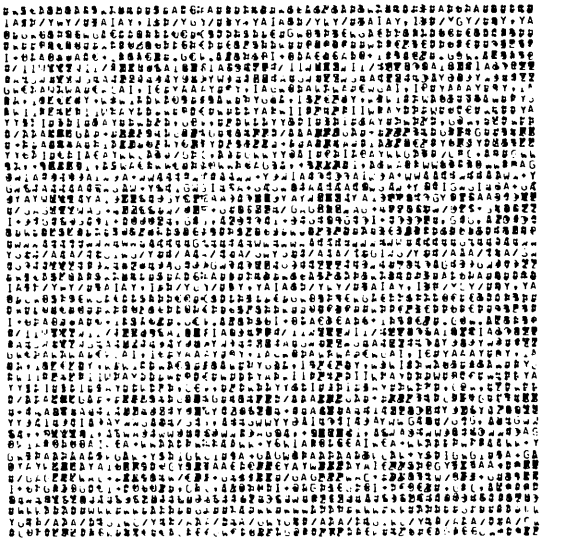

Fig. 18. 1 MeV image of Au split interstitial with relaxation ($u = 1{\cdot}097$ Å^{-1}; $\varepsilon = -455$ Å).

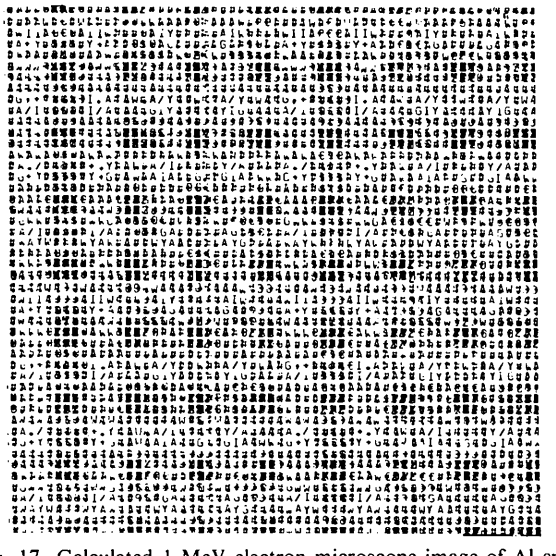

Fig. 17. Calculated 1 MeV electron microscope image of Al split interstitial with relaxation ($u = 1{\cdot}1$ Å^{-1}; $\varepsilon = -530$ Å).

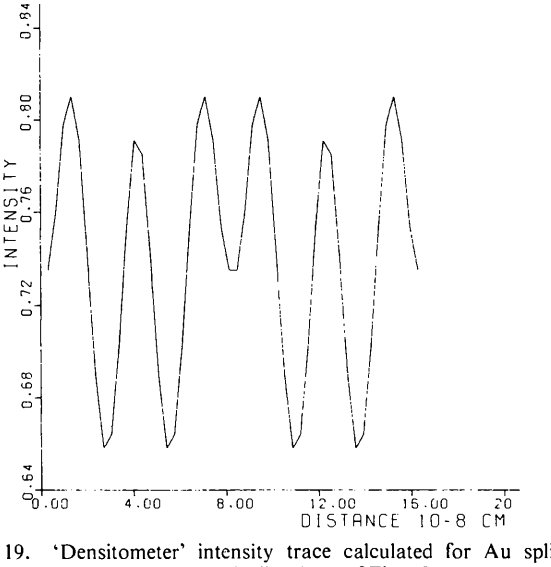

Fig. 19. 'Densitometer' intensity trace calculated for Au split interstitial along the line $(x, \frac{1}{2})$ of Fig. 10.

Table 1. *Contrast (%) for defects*

	Resolution: 2·2 Å				Resolution: 0·91 Å			
	Al		Au		Al		Au	
	Interstitial	Relaxation	Interstitial	Relaxation	Interstitial	Relaxation	Interstitial	Relaxation
100 keV	3	4	24	32	24	27	80	79
1 MeV	4	4	10	23	24	21	91	84

4. Discussion

The value of higher-voltage electron microscopy is clearly illustrated by the results. In addition to the increased resolution due to a more uniform transfer function out to larger reciprocal-space distances for constant spherical aberration, 1 MeV electron microscopy gives higher contrast and improved recognizability of atom structure. Contrast also increases with atomic number as expected from the dependence of electron scattering power on atomic number, and demonstrated by the values in Table 1. It is to be noted though that the higher mobility and formation energy for atomic defects in Au as compared to Al would require special experimental techniques, including low-temperature (<10 K) electron microscopy, and so the use of elements with high atomic number in studying atomic defect structures is not necessarily the automatic choice.

Based upon the preceding computational results, optimum experimental parameters necessary for the observation of split interstitials in f.c.c. metals can be stated. A compromise between high contrast and recognizability may be required, but in general there is easiest interpretation of defect structure with reasonable contrast at approximately −470 Å defocus in bright field and in −270 Å defocus in dark field (at 1 MeV) when the objective aperture is just inside the lowest-order Bragg beams. Highest contrast with reasonable recognizability occurs when Bragg reflections are included within the objective aperture and when the defocus is at that value of underfocus which minimizes perfect-crystal contrast.

These results have by no means exhausted the variation in instrumental or specimen parameters which might affect our conclusions. A few calculations were made in order to suggest the effects of other experimental parameters and controls. The results may be enumerated as follows: (1) the variation in visibility with crystal thickness is not significant, *e.g.* a 150 Å thickness was used with a single defect layer, and although the value of the optimum defocus was changed, the visibility was not reduced; (2) the chromatic aberration does not degrade the computed image quality for values of range of focus <50 Å; (3) the coefficient of spherical aberration is not significant in the range 1·0 mm < C_s < 1·8 mm; (4) computed image visibility and interpretation is sensitive to defocus, *i.e.* 2 Å increments could give discernible variations in some calculations; (5) defect-structure visibility persists in other zone-axis orientations; specifically, for the unit cell used in our calculations the [112] orientation (equivalent to the [111] cubic orientation) was computed, and the split interstitial was easily seen against the perfect-crystal close-packing arrangement.

We may conclude that for a wide range of experimental parameters and defect structure models, the dynamical diffraction calculations using the assumption of periodic continuation provide a very effective method for representing the diffuse scattering and electron-microscope image contrast for non-periodic structures.

References

ANSTIS, G. R. & O'KEEFE, M. A. (1976). *34th Ann. Proc. Electron Microsc. Soc. Am.* Edited by G. W. BAILEY, pp. 480–481. Baton Rouge, Louisiana: Claitors Publ. Div.

BOURRET, A., DESSEAUX, J. & RENAULT, A. (1975). *Acta Cryst.* A**31**, 746–752.

COCKAYNE, D. J. H. (1976). *Electron Microscopy* 1976 (*Proc. Sixth Eur. Cong. Electron Microsc.*), Vol. 1, Edited by D. G. BRANDON, pp. 109–113. Jerusalem: Tal International.

COWLEY, J. M. (1975*a*). *Microscopie Electronique à Haute Tension* 1975, Edited by B. JOUFFREY and P. FAVARD, pp. 129–134. Paris: Société Française de Microscopie Electronique.

COWLEY, J. M. (1975*b*). *Diffraction Physics*. Amsterdam: North-Holland.

COWLEY, J. M. & MOODIE, A. F. (1957). *Acta Cryst.* **10**, 609–619.

COWLEY, J. M. & MURRAY, R. J. (1968). *Acta Cryst.* A**24**, 329–336.

CREWE, A. V., WALL, J. & LANGMORE, J. P. (1970). *Science*, **168**, 1138–1140.

FEJES, P. L. (1973). PhD Thesis, Arizona State Univ.

FISHER, P. M. J. (1965). *Proc. Int. Conf. Electron Diffraction and Crystal Defects*, Australian Academy of Science, paper 1H-4.

GOODMAN, P. & MOODIE, A. F. (1974). *Acta Cryst.* A**30**, 280–290.

GRINTON, G. R. & COWLEY, J. M. (1971). *Optik*, **34**, 221–233.

HASHIMOTO, H., ENDOH, H., TANJI, T., ONO, A. & WATANABE, E. (1977). *J. Phys. Soc. Jpn.* In the press.

HAUBOLD, H. G. (1975). *J. Appl. Cryst.* **8**, 175–183.
IIJIMA, S. (1976). *34th Ann. Proc. Electron Microsc. Soc. Am.* Edited by G. W. BAILEY, pp. 490–491. Baton Rouge, Louisiana: Claitors Publ. Div.
IIJIMA, S. (1977). *Optik.* **43**, 193–214.
KRAKOW, W., CHANG, A. L. J. & SASS, S. L. (1977). *Philos. Mag.* In the press.
KUWABARA, S. & UEFUJI, T. (1975). *J. Electron Microsc.* **24**, 137–144.
SKARNULIS, A. J. (1975). PhD Thesis, Arizona State Univ.
SKARNULIS, A. J., IIJIMA, S. & COWLEY, J. M. (1976). *Acta Cryst.* A**32**, 799–805.
SPENCE, J. C. H. (1975). *Developments in Electron Microscopy and Analysis*, Edited by J. A. VENABLES, p. 257. New York: Academic Press.
SPENCE, J. C. H. (1977). In *35th Ann. Proc. Electron Microsc. Soc. Am.* Edited by G. W. BAILEY, pp. 178–179. Baton Rouge, Louisiana: Claitors Publ. Div.

Acta Cryst. (1978). A**34**, 112–116

Approximations for Dynamical Calculations of Microdiffraction Patterns and Images of Defects

BY JOHN C. H. SPENCE

Arizona State University, Department of Physics, Tempe, Arizona 85281, *USA*

(*Received* 3 *March* 1977; *accepted* 15 *August* 1977)

The calculation of dynamical elastic diffuse electron scattering from a crystal containing a point defect or dislocation may require prohibitively large amounts of computing time. Two approximations are described which greatly reduce the computer time required for these calculations, and so allow the simulation of electron-microscope images of defects at atomic resolution. The diffuse scattering expected from microdiffraction experiments can also be predicted in this way.

1. Introduction

Recent instrumental developments in high-resolution transmission electron microscopy have led to the production of a generation of instruments capable of producing high-quality images showing a point resolution of perhaps 3·5 Å and, in favorable cases, lattice resolution better than 1·0 Å. Image detail from metallurgical specimens on this scale cannot be interpreted with the conventional theory of diffraction contrast from imperfect crystals based on the column approximation (see, for example, Hirsch, Howie, Nicholson, Pashley & Whelan, 1965). The most recent development of this theory, the weak-beam method, allows an interpretation of detail on electron micrographs down to perhaps 15 Å. Despite the considerable success of diffraction contrast theory for the characterization of dislocations and the investigation of their interactions, much recent interest has centered on the development of theoretical methods to allow the fullest use of present-day instrumental capabilities. Rather than obtaining contrast from the defect strain field in a single-beam image as in conventional metallurgical microscopy, the aim is to use the methods of lattice imaging (Menter, 1956; Cockayne, Parsons & Hoelke, 1971; Iijima, 1975) and single-atom imaging (Hashimoto, Kumao, Hino, Yotsumoto & Ono, 1973) to expose the structure of the defect at high resolution. There is some hope that by matching computer-simulated trial structure images and diffraction patterns with experimental recordings, the detailed atomic structure of a defect may be revealed. The necessary experimental images and diffraction patterns can now be recorded under closely specified experimental conditions with, for the image, known values of defocus, spherical and chromatic aberration constants, incident-beam divergence and specimen orientation (see, for example, Krivanek, 1976).

Experience in our laboratory has shown that the computer simulation of these high-resolution electron images requires very large amounts of computer time. For example, a recent 500-beam dynamical calculation showing through-focus images from an interstitial defect in a lead film (thickness 80 Å) required 10 min computing time on a Univac 1110-42 computer. This raises serious questions about the usefulness of image simulation as a tool for the structure analysis of defects.

The purpose of this note is to outline two approximations which can be made to reduce the amount of computing time required by use of the multislice method. Methods for calculating the coherent scattering from non-periodic specimens have been known for some time in X-ray diffraction (see, for example, Krivoglaz & Ryaboshapka, 1963); however, calculations for electron scattering where dynamical scattering may be important are a more recent development (Grinton & Cowley, 1971; Cockayne, 1976).